Physical insight and performance metrics of monolayer MX_2 heterojunction TFETs

Khairul Alam ✉

Department of Electrical and Electronic Engineering, East West University, Dhaka-1212, Bangladesh
✉ *E-mail: kalam@ewubd.edu*

Published in Micro & Nano Letters; Received on 29th September 2019; Revised on 30th October 2019; Accepted on 6th November 2019

The physics and performance of monolayer MX_2 heterojunction n TFETs are studied using a quantum simulation. The imaginary wave vector reveals that WTe_2 is the most promising source material. Results of heterojunction TFETs with WTe_2 source material and of WTe_2 homojunction TFET reveal that WTe_2–MoS_2 heterojunction TFET is the most promising candidate with a 620 μA/μm drive current for a 0.3 volt gate swing. The energy gap between the valence band of source material and the conduction band of channel material, δE_{cv}, is the key parameter for high drive current. The WTe_2–MoS_2 heterojunction has the smallest δE_{cv} value that results in small band bending near the heterojunction, which creates the shortest tunnel path and therefore yields the highest drive current. The WTe_2–MoS_2 TFET has an average turn-on slope of 15.6 mV/dec, an on/off current ratio of 6.2×10^8, a drive current of 620 μA/μm, a transconductance of 10.98 mS/μm, a total capacitance of 0.829 fF/μm, a switching delay of 0.401 ps, and a cutoff frequency of 2.1 THz. The performance metrics closely comply with the ITRS 2026 LOP and LSTP device requirements. Its I_{60} value of 11.97 μA/μm is large enough to compete with MOSFETs.

1. Introduction: Increased power dissipation in nanoscaled transistors may be overcome by tunnelling field-effect transistors (TFETs) due to their sub-60 mV/dec turn-on characteristics, which allows aggressive V_{DD} scaling [1–4]. Transition metal dichalcogenides (TMDCs) are layered materials. Monolayer and a few layers of TMDCs have been used to implement field effect transistors [5, 6]. The bulk and few layers of TMDCs have an indirect bandgap. Therefore, they are not promising candidates for band to band tunnelling (BTBT) transistors. However, the monolayer TMDCs are direct gap two-dimensional (2D) materials [7, 8]. Different techniques such as mechanical exfoliation [9, 10] and lithium-based intercalation [11] can be used to extract a monolayer from the bulk metal chalcogenides family.

Superior performance of TMDC heterojunction (HTJ) TFETs over their homojunction (HJ) counterparts has been reported by Cao *et al.* [4]. According to their simulation study, WTe_2 and MoS_2 are the best combination. An experimental demonstration of BTBT in MoS_2-MoTe_2 HTJ has been reported in [12]. They have found that the staggered band alignment at the hetero-interface boosts the BTBT compared to the HJ configuration. Vertical HTJ WTe_2 and MoS_2 TFETs are studied in [13]. Their results show that the ultra-steep turn-on characteristic is robust against atomic defects and impurity scattering. Lam *et al.* [14] reported an order of magnitude enhancement in on-state current for the common- X HTJ TFETs compared to the constituents' HJ TFETs. Choukroun *et al.* [15] compared several HTJs and reported that WTe_2-MoS_2 and $MoTe_2-MoS_2$ are the most promising HTJs.

Monolayer TMDCs have been used to realise TFETs both in vertical tunnelling structure [13, 16–20] and lateral tunnelling structure [12, 14, 15, 21, 22]. However, the lateral structure is conventional and the experimental technique of the lateral structure is rapidly growing [23–26]. Although lateral HTJ TFETs of different combinations of monolayer TMDCs have been studied [4, 13–15] and a few combinations such as WTe_2-MoS_2 and $MoTe_2-MoS_2$ have been reported as the most promising combinations, the deep level physical insight of such combinations needs to be understood and the benchmark of their device performance against the technology requirements need to be assessed. In this work, we choose lateral HTJ TFETs of monolayer TMDC to understand the physical insight of BTBT in such structures and to evaluate the performance metrics of such a TFET. We also benchmark its performance metrics against the ITRS 2026 low operating power (LOP) and low standby power (LSTP) technology requirements [27].

2. Device structure and simulation approach: The double gate TFET device structure that we use for simulation is shown in Fig. 1*a*. The gate oxide is HfO_2 with a dielectric constant of 20 and a thickness value of 2.56 nm. This is equivalent to an effective oxide thickness of 0.5 nm. The source and drain are doped with a doping density of 10^{21} and 5×10^{20} cm^{-3}, respectively, and the channel is intrinsic. The effective doping can be done by surface adatoms [28] and absorption of atoms such as potassium [29], rhenium [30], gold [30], niobium [31], chlorine [32], and hydrogen [32, 33]. The monolayer MX_2 HTJ is formed at the source–channel interface with a staggered band alignment as schematically shown in Fig. 1*b*. The monolayer MX_2 materials used for source, drain, and channel have hexagonal honeycomb lattice structures (1H-MX_2), which are semiconductors and have a finite gap at the K-point of the 2D hexagonal Brillouin zone (BZ). The source is a lower bandgap MX_2 while the channel MX_2 has a relatively higher bandgap. The source–channel HTJ uses monolayer MX_2 with different combinations.

For simulation, we solve Poisson's equation and non-equilibrium Green's functions (NEGF) self-consistently. The 2D Poisson's equation uses a finite difference scheme for discretisation over the entire device domain and is solved using a Newton–Rapshon method. Discretisation uses a 0.2 nm grid in the channel and a 0.5 nm grid in oxide and other parts of the device domain. Under boundary conditions, we fixed the voltage at gate electrodes and set the normal component of electric field to zero at all other boundaries. We use a recursive Green's function algorithm (RGFA) [34] to solve NEGF for electron and hole densities under ballistic transport

$$n(x, z) = n_s n_v \int_{-\infty}^{\infty} \mathrm{d}k_y \int_{E_C}^{\infty} \frac{\mathrm{d}E}{2\pi} [A_S(E, k_y) f(E, k_y, \mu_S) + A_D(E, k_y) f(E, k_y, \mu_D)], \quad (1)$$

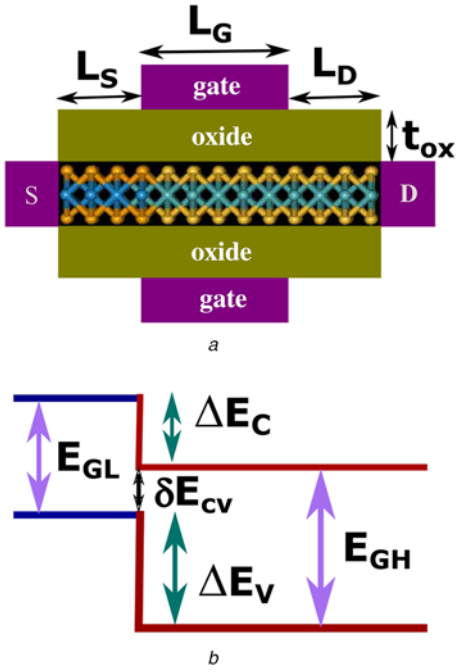

Fig. 1 *The schematics of device cross section and heterojunction band alignment*
a Cross section of the TFET structure used for simulation. The channel is an axial hetero-structure of MX_2 2D material. Different dimensions are $L_S = L_G = L_D = 20$ nm and $t_{ox} = 2.56$ nm, which is corresponding to an effective oxide thickness of 0.5 nm
b Sketch of staggered band alignment along the transport direction. E_G's are the band gaps of low- and high-bandgap materiials, ΔE_C and ΔE_V are the conduction and valence band offsets, and δE_{cv} is the offset between valence band of low-bandgap material and conduction band of high-bandgap material

$$p(x,z) = n_s n_v \int_{-\infty}^{\infty} dk_y \int_{-\infty}^{E_V} \frac{dE}{2\pi} [A_S(E,k_y)(1-f(E,k_y,\mu_S)) + A_D(E,k_y)(1-f(E,k_y,\mu_D))]. \quad (2)$$

Here n_s and n_v account for spin and valley degeneracies, respectively, A's are the source and drain spectral functions, f is the Fermi function, and μ's are the source and drain Fermi levels. The RGFA and calculation procedures of A_S and A_D are discussed in detail in [34, 35]. The BZ of monolayer MX_2 is hexagonal, and the band edges happen at the K-points of the BZ. As there are six K-points in the hexagonal BZ and each K-point is shared by three adjacent units, we set n_v to 2.

The monolayer MX_2 is modelled using a two-band Hamiltonian at K-point [36]

$$H(k_x,k_y) = \begin{bmatrix} E_C & tf(k_x,k_y) \\ tf^*(k_x,k_y) & E_V \end{bmatrix}, \quad (3)$$

where E_C and E_V represent the band edges, $t = (\hbar/a)\sqrt{2E_G/2m^*}$, and $f(k_x, k_y)$ is given by

$$f(k_x,k_y) = \exp\left(\frac{ik_y a}{\sqrt{3}}\right) + 2\exp\left(-\frac{ik_y a}{2\sqrt{3}}\right)\cos\left(\frac{k_x a}{2}\right). \quad (4)$$

The lattice constant a, the bandgap E_G at K-point and the effective mass m^* are taken from [37]. The strain is not considered in this work. The source and channel are modelled using their unstrained Hamiltonians, and the interface coupling matrix is the average of the two.

The self-consistent loop starts with an initial guess of the potential profile based on the equilibrium calculation. The potential update for subsequent iterations uses an Anderson mixing scheme [38] to expedite the convergence. Once the profile is converged, the direct BTBT current is calculated from

$$I_D = n_s n_v \left(\frac{e}{\hbar}\right) \int_{-\infty}^{\infty} dk_y \int_{-\infty}^{\infty} \frac{dE}{2\pi} T(E,k_y) \cdot [f(E,k_y,\mu_S)) - f(E,k_y,\mu_D))], \quad (5)$$

where e is the electronic charge, $\hbar$ is the reduced Planck's constant, and we use RGFA [34, 35] to calculate the transmission coefficient

$$T = \mathrm{tr}(\Gamma^S_{1,1}[A_{1,1} - G_{1,1}\Gamma^S_{1,1}G^\dagger_{1,1}]), \quad (6)$$

where G is the retarded Green's function and Γ^S is the source broadening function [34, 35].

3. Results and discussions: The imaginary wave vector that connects the conduction band to the valence band through the energy gap is the key factor for evaluating the direct BTBT probability. As the current flow in a tunnel field-effect transistor is controlled by the direct BTBT, we first need to examine the imaginary wave vector that connects the band edges of a monolayer MX_2. The imaginary wave vector versus energy curves of six monolayer MX_2 materials is shown in Fig. 2. The solid lines are for $M = W$ and the corresponding dashed lines are for $M = M_o$. The area under the imaginary wave vector curve has an inverse relation with the direct BTBT probability. The lesser the area is, the more the tunnelling probability is. Clearly, WTe_2 has the highest tunnelling probability as it has the lowest area. Taking WTe_2 as the reference, the area ratios for Mo materials are MoS_2:$MoSe_2$:$MoTe_2$ = 4.03:3.46:2.11, and for W materials are WS_2:WSe_2:WTe_2 = 3.06:2.29:1. Therefore, as source material, the best choice is obviously WTe_2, the next one is $MoTe_2$, and so on.

First, a TFET is well known to have bipolar characteristics, i.e. current flows for both positive and negative gate biases. Second, a TFET generally has a poor drive current. One of the effective ways to block the bipolar characteristics and to boost the drive current is to use a source–channel HTJ [12, 14, 20, 39, 40] with a staggered band alignment. As WTe_2 has the highest BTBT probability (the lowest area of the imaginary wave vector curve), we choose WTe_2–WS_2 HTJ for the same M, WTe_2–$MoTe_2$ HTJ for the same X, and WTe_2–MoS_2 mixed HTJ. In all three cases, the HTJ band alignment is TYPE-II as shown in Fig. 1*b* and WTe_2 is the source material for the highest possible drive current. We took the band alignment parameters, ΔE_C and ΔE_V from [41].

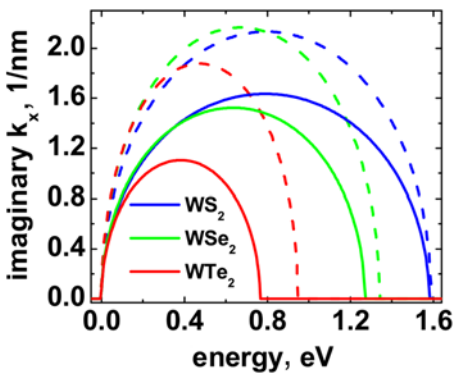

Fig. 2 *Imaginary wave vector k_x versus energy plots for six monolayer MX_2 materials. The solid lines are for $M = W$ and the corresponding dashed lines are for $M = Mo$. The valence band top is the reference energy*

doi: 10.1049/mnl.2019.0588

The drain current, I_D, versus the gate bias, V_{GS}, characteristics for three HTJ together with the WTe_2 HJ channels are shown in Fig. 3. We set drain bias, V_{DS} to 0.3 V and swing V_{GS} over a wide range. Then the I–V curves are shifted along the voltage axis to set $V_{GS} = 0$ at $I_D = 10^{-6}$ μA/μm. Note that the bipolar part (negative V_{GS}) of the HJ channel is not shown in the figure for better visibility. In terms of on-state current and turn-on slope, the WTe_2–$MoTe_2$ HTJ TFET and the WTe_2 HJ TFET have very similar characteristics, whereas, WTe_2–MoS_2 and WTe_2–WS_2 HTJ TFETs have improved characteristics. As off-state is set at $I_D = 10^{-6}$ μA/μm and $V_{GS} = 0$, we defined on-state as $V_{GS} = V_{DS} = 0.3$ V, and found that the on-state currents are, respectively, 620, 7.6, 0.63, and 0.43 μA/μm for WTe_2–MoS_2 HTJ, WTe_2–WS_2 HTJ, WTe_2–$MoTe_2$ HTJ, and WTe_2 HJ TFETs. The corresponding average turn-on slopes are 15.6, 17.8, 28.3, and 31.3 mV/dec over the drain current range of 10^{-6} to 10^{-2} μA/μm. Clearly, the WTe_2–$MoTe_2$ HTJ and the WTe_2 HJ TFETs have similar turn-on and on-state behaviour. However, the on-state current of WTe_2–MoS_2 TFET is far better than other three TFETs, although its turn-on slope is close to that of WTe_2–WS_2 TFET, i.e. the WTe_2–MoS_2 HTJ has the highest drive current with an on/off current ratio of 6.2×10^8 for a 0.3 V swing. Lam *et al.* [14] simulated various HJ and HTJ TFETs and reported that $MoTe_2$–WTe_2 HTJ has the highest drive current for p-TFET and WTe_2 HJ is best for n-TFET. The HTJ combinations that have been used for n-TFETs are WS_2–MoS_2, WSe_2–$MoSe_2$, and WTe_2–$MoTe_2$, i.e. MX_2 HTJs with the same X. However, Cao *et al.* [4] reported that WTe_2–MoS_2 is the best HTJ combination, which is consistent with our results. Lateral HTJs of WTe_2–MoS_2 and $MoTe_2$–MoS_2 have also been reported as the most promising combinations [15]. Li *et al.* [20] reported very steep turn-on characteristics of WTe_2–MoS_2 vertical HTJ.

To understand the physics behind the high drive current in WTe_2–MoS_2 HTJ TFET, we plot the on-state electric field distribution along the channel in Fig. 4 and the band profiles together with the current spectrum in Fig. 5. The HTJ is located at $x = 0$. The negative electric field in Fig. 4 indicates that the electrons move in the positive x direction (from source to drain). The electric field magnitude at the WTe_2–WS_2 junction is 15.77 MV/cm and it is 11.46 MV/cm at WTe_2–MoS_2 junction, i.e. in on-state, the junction field value is higher at WTe_2–WS_2 junction. Clearly, the electric field is not the origin of the high drive current of WTe_2–MoS_2 HTJ.

From current density profiles of Fig. 5 we see that WTe_2–MoS_2 HTJ TFET has a peak current density of 8.65×10^3 μA/μm/eV at energy $E = -0.093$ eV (source Fermi level is the reference). The tunnel path at this energy is 1.93 nm long, whereas, the WTe_2–WS_2 HTJ TFET has the peak current density of 67.6 μA/μm/eV and the corresponding tunnel path is 5.74 nm long. Clearly, the shortest tunnel path results in high drive current

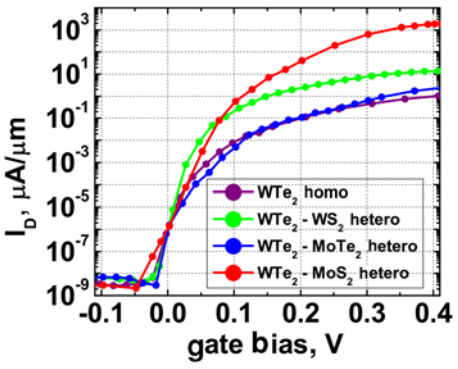

Fig. 3 *Drain current versus gate bias plots for MX_2 homo and hetero junction n-channel TFETs. The drain to source bias $V_{DS} = 0.3$ V*

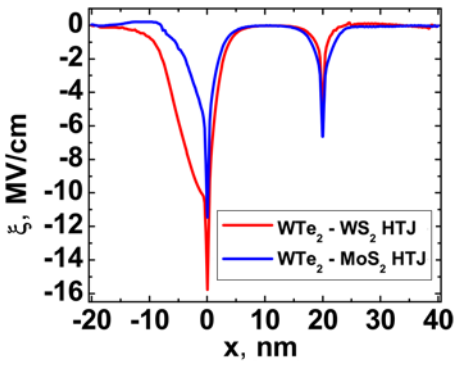

Fig. 4 *On-state electric field along the transport direction of WTe_2–MoS_2 and WTe_2–WS_2 HTJ TFETs*

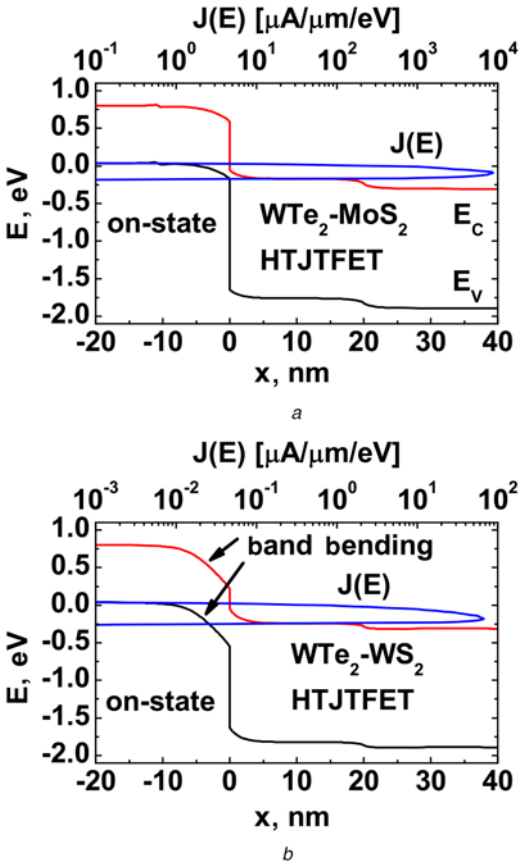

Fig. 5 *On-state band profiles and current spectrum*
a WTe_2–MoS_2 HTJ TFET
b WTe_2–WS_2 HTJ TFET. Source Fermi level is the energy reference

in WTe_2–MoS_2 HTJ TFET. Despite the same source material and same type (TYPE-II) of band alignment, a longer tunnel path is created in WTe_2–WS_2 junction due to the high junction field (see Fig. 4). The high junction field creates larger band bending near the junction (see two arrows in Fig. 5*b*) which results in longer tunnelling path.

To gain further insight into the physics of high drive current in WTe_2–MoS_2 HTJ TFET, we look into the band alignment again. We denoted the energy gap between the conduction band of the channel material and the valence band of the source material as δE_{cv} as shown in Fig. 1*b*. Taking WTe_2 as the source material in all HTJs, the δE_{cv} values for MoS_2, $MoSe_2$, $MoTe_2$, WS_2, and WSe_2 are, respectively, 0.13, 0.51, 0.60, 0.51, and 0.82 eV [41]. The lowest value of δE_{cv} in WTe_2–MoS_2 HTJ is the origin for

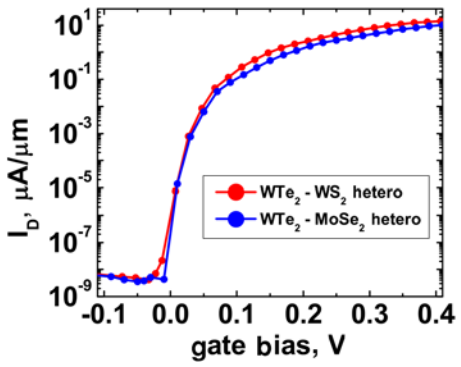

Fig. 6 *Comparison of I–V characteristics of WTe_2–WS_2 and WTe_2–$MoSe_2$ HTJ TFETs. Both HTJs have the same δE_{cv} value*

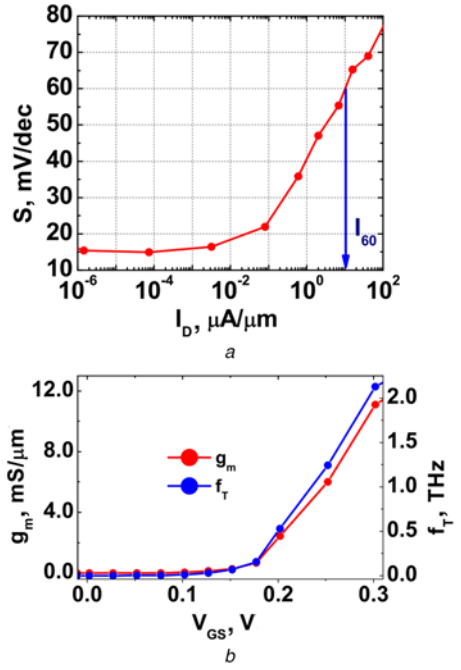

Fig. 7 *Turn-on slope, transconductance, and cut-off frequency plots*
a Subthreshold slope versus drain current plot
b Transconductance g_m and cut-off frequency f_T versus gate bias plots for the WTe_2–MoS_2 HTJ TFET

lower on-state electric field, which results in the shortest tunnel path. The origin can be further verified from the values of δE_{cv}. We see that both the WTe_2–WS_2 and WTe_2–$MoSe_2$ HTJs have the same δE_{cv} values. Therefore, both TFETs should have very similar *I–V* characteristics. This is, in fact, the case. The results are compared in Fig. 6. The slight difference may come from different dielectric values of WS_2 and $MoSe_2$.

After gaining the insight of high current in WTe_2–MoS_2 HTJ TFET, we next evaluate the performance metrics of this structure. For a 0.3 V swing in V_{GS}, we find that the on-state current is 620 μA/μm, which is corresponding to an on/off current ratio of 6.2×10^8. The subthreshold slope S, transconductance g_m, and unity current gain frequency f_T are shown in Fig. 7. The subthreshold slope S is below 60 mV/dec over seven decades change in current. The average $S = 15.6$ mV/dec in the I_D range of 10^{-6}–10^{-2} μA/μm. A reference independent figure of merit for sub-60 mV/dec devices is I_{60}, i.e. the drain current at 60 mV/dec. According to Vandenberghe *et al.* [42], the I_{60} value of a HJ TFET should be in the range of 1–10 μA/μm to compete with metal oxide semiconductor field effect transistors (MOSFETs).

Table 1 Benchmarking performance metrics of WTe_2–MoS_2 HTJ TFET against ITRS requirements for 2026 LOP and LSTP devices

Parameter	WTe_2–MoS_2 TFET	2026 LOP FET	2026 LSTP FET
I_{on}, μA/μm	620	666	286
I_{on}/I_{off}	6.2×10^8	1.3×10^5	2.86×10^7
S, mV/dec	15.6	—	—
g_m, mS/μm	10.98	—	—
C_f, fF/μm	0.194	0.18	0.18
C_{tot}, fF/μm	0.829	0.402	0.383
τ_s, ps	0.401	0.26	0.73
CV^2, fJ/μm	0.0746	0.07	0.11

From Fig. 7*a*, we see that the I_{60} value is 11.97 μA/μm, which is large enough to battle against the MOSFET competitor. The transconductance plotted in Fig. 7*b* is also high due to high drive current. The on-state value of transconductance is $g_m = 10.98\,\text{mS}/\mu\text{m}$, which is significantly higher than its 60 mV/dec competitors MoS_2 and Si ultra-thin body MOSFETs [43].

The gate capacitance has the components of oxide capacitance, quantum capacitance, and fringing field capacitance. While the quantum capacitance is computed from $\delta Q_{ch}/\delta\phi_s$, where Q_{ch} is the channel charge and ϕ_s is the surface potential, the fringing field capacitance is obtained from

$$C_f = \epsilon_{ext} \frac{\partial}{\partial V_{GS}} \int dz \left[\mathcal{E}_{GS}(z) + \mathcal{E}_{GD}(z)\right]. \quad (7)$$

Here, $\mathcal{E}_{GS}(z)$ and $\mathcal{E}_{GD}(z)$ are the electric field components in the axial direction that come out of the gate metal towards the source and drain contacts, respectively, and ϵ_{ext} is the dielectric constant of the extended dielectric. The fringing field capacitance in parallel with the series combination of the quantum and oxide capacitances gives the total gate capacitance C_g. The unity current gain frequency (or cut-off frequency) calculated from $f_T = g_m/2\pi C_g$ is shown in Fig. 7*b*. The on-state value of f_T is 2.1 THz. The switching delay time obtained from $\tau_s = C_g V_{DD}/I_{on}$ is 0.401 ps in on-state. In Table 1, we benchmark the performance metrics of WTe_2–MoS_2 HTJ TFET against the ITRS requirements for 2026 LOP logic and LSTP logic. Although the gate capacitance and the delay time are slightly high, the dynamic power dissipation (CV^2) meets the requirement.

4. Conclusion: In conclusion, we have performed simulation studies of monolayer MX_2 HJ and HTJ tunnel FETs. The complex band structures of different MX_2 monolayer materials show that WTe_2 is the most promising source material for BTBT. Simulation results of different HTJ structures with WTe_2 as the source material and of the WTe_2 HJ structure show that the WTe_2–MoS_2 HTJ TFET supplies the highest drive current. The energy gap between the valence band of WTe_2 and the conduction band of MoS_2 is very small. Therefore, band alignment for BTBT happens at the junction at a relatively lower electric field. This results in small band bending near the HTJ which creates the shortest tunnel path and hence the highest drive current. The WTe_2–MoS_2 HTJ TFET has high on-current, high transconductance, and very low subthreshold slope that meet the ITRS 2026 LOP requirements. However, the switching delay is slightly larger due to the high gate capacitance.

5 References

[1] Gopalakrishnan K., Griffin P.B., Plummer J.D.: 'I-MOS: a novel semiconductor device with a subthreshold slope lower than kT/q'. Int. Electron Devices Meeting, San Francisco, CA, USA, 8–11 December 2002, pp. 289–292

doi: 10.1049/mnl.2019.0588

[2] Seabaugh A., Zhang Q. 'Low-voltage tunnel transistors for beyond CMOS logic', *Proc. IEEE*, 2010, **98**, pp. 2095–2110

[3] Ionescu A.M., Riel H.: 'Tunnel field-effect transistors as energy efficient electronic switches', *Nature*, 2011, **479**, (7373), pp. 329–337

[4] Cao W., Jiang J., Kang J., *ET AL.*: 'Designing band-to-band tunneling field-effect transistors with 2D semiconductors for next-generation low-power VLSI'. Int. Electron Devices Meeting, Washington, DC, USA, 7–9 December 2015, pp. 305–308

[5] Radisavljevic B., Radenovic A., Brivio J., *ET AL.*: 'Single-layer MoS_2 transistors', *Nat. Nanotechnol.*, 2011, **6**, (3), pp. 147–150

[6] Qiu H., Pan L., Yao Z., *ET AL.*: 'Electrical characterization of back-gated bi-layer MoS_2 field-effect transistors and the effect of ambient on their performances', *Appl. Phys. Lett.*, 2012, **100**, p. 123104

[7] Kam K.K., Parkinson B.A.: 'Detailed photocurrent spectroscopy of the semiconducting group VIB transition metal dichalcogenides', *J. Phys. Chem.*, 1982, **86**, pp. 463–467

[8] Mak K.F., Lee C., Hone J., *ET AL.*: 'Atomically thin MoS_2: a new direct-gap semiconductor', *Phys. Rev. Lett.*, 2010, **105**, (13), p. 136805

[9] Frindt R.F.: 'Single crystals of MoS_2 several molecular layers thick', *J. Appl. Phys.*, 1966, **37**, pp. 1928–1929

[10] Chan A.S., Fu X., Panin G.N., *ET AL.*: 'Shear exfoliation and photoresponse of 2D-layered gallium selenide nanosheets', *Phys. Status Solidi-Rapid Res. Lett.*, 2018, **12**, pp. 18002261–18002264

[11] Schumacher A., Scandella L., Kruse N., *ET AL.*: 'Single-layer MoS_2 on mica: studies by means of scanning force microscopy', *Surf. Sci. Lett.*, 1993, **289**, pp. L595–L598

[12] Balaji Y., Smets Q., Rosa C.J.L.D.L., *ET AL.*: 'Tunneling transistors based on MoS_2/$MoTe_2$ van der Waals heterostructures', *J. Electron Device Soc.*, 2018, **6**, pp. 1048–1055

[13] Lam K.T., Seol G., Guo J.: 'Performance evaluation of MoS_2–WTe_2 vertical tunneling transistor using real-space quantum simulator'. Int. Electron Devices Meeting, San Francisco, CA, USA, 15–17 December 2014, pp. 721–724

[14] Lam K.T., Cao X., Guo J.: 'Device performance of heterojunction tunneling field-effect transistors based on transition metal dichalcogenide monolayer', *IEEE Electron Device Lett.*, 2013, **34**, (10), pp. 1331–1333

[15] Choukroun J., Pala M., Fang S., *ET AL.*: 'High performance tunnel field effect transistors based on in-plane transition metal dichalcogenide heterojunctions', *Nanotechnology*, 2019, **30**, pp. 0252011–02520111

[16] Szaboa A., Koesterb S.J., Luisier M.: 'Metal-dichalcogenide hetero-TFETs: are they a viable option for low power electronics?'. Device Research Conf., Santa Barbara, CA, USA, 22–25 June 2014, pp. 19–20

[17] Memisevic E., Svensson J., Hellenbrand M., *ET AL.*: 'Vertical InAs/GaAsSb/GaSb tunneling field-effect transistor on Si with $S = 48$ mV/decade and $I_{on} = 10\,\mu A/\mu m$ for $I_{off} = 1\,nA/\mu m$ at $v_{DS} = 0.3$ V. Int. Electron Devices Meeting, San Francisco, CA, USA, December 2016, pp. 3–7

[18] Lam K.T., Seol G., Guo J.: 'Operating principles of vertical transistors based on monolayer two-dimensional semiconductor heterojunctions', *Appl. Phys. Lett.*, 2014, **105**, (1), pp. 0131121–0131125

[19] Sarkar D., Xie X., Liu W., *ET AL.*: 'A subthermionic tunnel field-effect transistor with an atomically thin channel', *Nature*, 2015, **526**, pp. 91–95

[20] Li M.O., Esseni D., Snider G., *ET AL.*: 'Single particle transport in two-dimensional heterojunction interlayer tunneling field effect transistor', *J. Appl. Phys.*, 2014, **115**, (7), pp. 0745081–07450811

[21] Das S., Prakash A., Salazar R., *ET AL.*: 'Toward low-power electronics: tunneling phenomena in transition metal dichalcogenides', *ACS Nano*, 2014, **8**, (2), pp. 1681–1689

[22] Ilatikhameneh H., Tan Y., Novakovic B., *ET AL.*: 'Tunnel field-effect transistors in 2-D transition metal dichalcogenide materials', *IEEE J. Explor. Solid-State Comput. Devices Circuits*, 2015, **1**, pp. 12–18

[23] Huang C., Wu S., Sanchez A.M., *ET AL.*: 'Lateral heterojunctions within monolayer $MoSe_2$–WSe_2 semiconductors', *Nat. Mater.*, 2014, **13**, pp. 1096–1101

[24] Zhang X.Q., Lin C.H., Tseng Y.W., *ET AL.*: 'Synthesis of lateral heterostructures of semiconducting atomic layers', *Nano Lett.*, 2015, **15**, (1), pp. 410–415

[25] Son Y., Li M.Y., Cheng C.C., *ET AL.*: 'Observation of switchable photoresponse of a monolayer WSe_2–MoS_2 lateral heterostructure via photocurrent spectral atomic force microscopic imaging', *Nano Lett.*, 2016, **16**, (6), pp. 3571–3577

[26] Aras M., Kilic C., Ciraci S.: 'Lateral and vertical heterostructures of transition metal dichalcogenides', *J. Phys. Chem.*, 2018, **122**, (3), pp. 1547–1555

[27] (2012 PIDS Table). International Technology Roadmap for Semiconductors. Available at http://www.itrs2.net

[28] Fang H., Chuang S., Chang T.C., *ET AL.*: 'High-performance single layered WSe_2 p-FETs with chemically doped contacts', *Nano Lett.*, 2012, **12**, (7), pp. 3788–3792

[29] Fang H., Tosun M., Seol G., *ET AL.*: 'Degenerate n-doping of few-layer transition metal dichalcogenides by potassium', *Nano Lett.*, 2013, **13**, (5), pp. 1991–1995

[30] Lin Y.C., Dumcenco D.O., Komsa H.P., *ET AL.*: 'Properties of individual dopant atoms in single-layer MoS_2: atomic structure, migration, and enhanced reactivity', *Adv. Mater.*, 2014, **26**, pp. 2857–2861

[31] Suh J., Park T.E., Lin D.Y., *ET AL.*: 'Doping against the native propensity of MoS_2: degenerate hole doping by cation substitution', *Nano Lett.*, 2014, **14**, (12), pp. 6976–6982

[32] Kim Y., Jhon Y.I., Park J., *ET AL.*: 'Plasma functionalization for cyclic transition between neutral and charged excitons in monolayer MoS_2', *Sci. Rep.*, 2016, **6**, p. 21405

[33] Oh S., Lim J.Y., Im S., *ET AL.*: 'Stability, efficiency, and mechanism of n-type doping by hydrogen adatoms in two-dimensional transition metal dichalcogenides', *Phys. Rev. B*, 2019, **100**, (10), pp. 2469–9950

[34] Lake R., Klimeck G., Bowen R.C., *ET AL.*: 'Single and multiband modeling of quantum electron transport through layered semiconductor devices', *J. Appl. Phys.*, 1997, **81**, (12), pp. 7845–7869

[35] Alam K., Lake R.K.: 'Leakage and performance of zero-Schottky-barrier carbon nanotube transistors', *J. Appl. Phys.*, 2005, **98**, p. 064307

[36] Peng B., Zheng W., Qin J., *ET AL.*: 'Two-dimensional MX_2 semiconductors for sub-5 nm junctionless field effect transistors', *Materials*, 2018, **11**, (30), pp. 4301–4309

[37] Kormanyos A., Burkard G., Gmitra M., *ET AL.*: 'K·p theory for two-dimensional transition metal dichalcogenide semiconductors', *2D Mater.*, 2015, **2**, p.022001

[38] Eyert V.: 'A comparative study on methods for convergence acceleration of iterative vector sequences', *J. Comput. Phys.*, 1996, **124**, (0059), pp. 271–285

[39] Roy T., Tosun M., Hettick M., *ET AL.*: '2D-2D tunneling field-effect transistors using WSe_2/$SnSe_2$ heterostructures', *Appl. Phys. Lett.*, 2016, **108**, (8), pp. 0831111–0831115

[40] Ganapathi K., Salahuddin S.: 'Heterojunction vertical band-to-band tunneling transistors for steep subthreshold swing and high ON current', *IEEE Electron Device Lett.*, 2011, **32**, (5), pp. 689–691

[41] Kang J., Tongay S., Zhou J., *ET AL.*: 'Band offsets and heterostructures of two-dimensional semiconductors', *Appl. Phys. Lett.*, 2013, **102**, (1), pp. 0121111–0121114

[42] Vandenberghe W.G., Verhulst A.S., Soree B., *ET AL.*: 'Figure of merit for and identification of sub-60 mV/decade devices', *Appl. Phys. Lett.*, 2013, **102**, (1), pp. 0135101–0135104

[43] Alam K., Lake R.K.: 'Monolayer MoS_2 transistors beyond the technology road map', *IEEE Trans. Electron Devices*, 2012, **59**, (12), pp. 3250–3254